Semarak Engineering Journal

Journal homepage:
https://semarakilmu.my/index.php/sej/index
ISSN: 3036-0145

CFD Study for CO2–KOH Reactive Absorption in a Bubble Column Reactor

Suci Madhania[1,*], Sugeng Winardi[1], Kusdianto[1], Mohammad Irwan Fatkhur Rozy[1], Latif Setyabudi[1], Christian Charisteo Wibisono[1], Putu Neo Sathya Devala[1]

[1] Department of Chemical Engineering, Faculty of Industrial Technology and System Engineering, Institut Teknologi Sepuluh Nopember Surabaya, Indonesia

ARTICLE INFO

Article history:
Received 25 June 2026
Received in revised form 3 July 2026
Accepted 10 July 2026
Available online 24 August 2026

Keywords:
Bubble Column Reactor; CFD; Interphase Mass Transfer; Reactive Absorption

ABSTRACT

Carbon dioxide capture through reactive absorption is a promising approach for mitigating industrial CO_2 emissions. This study investigates transient CO_2 absorption into aqueous KOH in a semi-batch bubble column using an integrated Computational Fluid Dynamics (CFD) framework that combines a Eulerian multiphase formulation, interfacial-force closures, Higbie penetration theory for liquid-side mass transfer, and a reaction enhancement factor. The framework was quantitatively validated against the experimental normalized CO_2 breakthrough response, showing close agreement with an R^2 of 0.986 and an RMSE of 0.003. The validated framework was subsequently used to interpret the spatial coupling among hydrodynamics, interfacial transport, and reactive absorption. Under the investigated bubbly-flow condition, the model predicted an average gas holdup of 0.089, an interfacial area of 177.8 m^{-1}, and a spatially averaged interphase mass-transfer coefficient of 0.0065 m/s. The simulation further predicted an aqueous $KHCO_3$ concentration of 0.0395 mol/L during absorption. Following product recovery by evaporation at 110 °C, X-ray diffraction identified K_2CO_3 as the dominant crystalline phase with minor $KHCO_3$ reflections, consistent with partial carbonate–bicarbonate transformation during recovery, while scanning electron microscopy revealed well-faceted prismatic particles with an average size of 3.42 ± 1.89 µm. The solid-phase characterization provides complementary post-recovery evidence rather than direct validation of the CFD-predicted internal fields. Overall, the study demonstrates the value of an experimentally constrained, engineering-scale CFD framework for mechanistically interpreting the coupling between bubble-column hydrodynamics, mass transfer, and reaction during transient CO_2–KOH absorption.

1. Introduction

Owing to its effect on climate change and global warming, the development of CO_2 absorption technology has become an important concern [1]. Generally, CO_2 is formed through post-combustion processes during energy production, as well as being present as an impurity of gas mixtures. The industry standard commonly uses aqueous solutions of alkanolamines for this purpose due to its high CO_2 absorption capacity, 0.45 mol CO_2/mol amine [2]. Nevertheless, alkanolamine absorption faces

* *Corresponding author.*
E-mail address: suci@its.ac.id

https://doi.org/10.37934/sej.15.1.257278

a significant challenge due to its considerable solvent regeneration energy requirement, estimated at approximately 10 – 14 MJ/kg CO_2 [3]. Therefore, aqueous potassium hydroxide (KOH) is considered in the present study as an alternative alkaline absorbent because its strong alkalinity promotes rapid reactive uptake of CO_2 and subsequent formation of carbonate and bicarbonate species [4].

Bubble column reactors are commonly recognized as apparatuses for gas–liquid processing [5]. In these reactors, the gas is introduced through a distributor as the dispersed phase, whereas the liquid constitutes the continuous phase [6]. Bubble columns offer several advantages, including the absence of moving parts, simple and compact structure, low operating and maintenance costs, as well as a high interfacial area that provides superior mass transfer and reaction performance [7], [8]. These characteristics are particularly relevant to reactive CO_2 absorption, in which reactor hydrodynamics determine bubble distribution, gas holdup, gas–liquid interfacial area, and ultimately the rate at which CO_2 is transferred to and consumed within the alkaline liquid phase. In the CO_2–KOH system, the absorbed CO_2 may subsequently be converted into carbonate and bicarbonate species, linking gas–liquid transport directly to liquid-phase reaction chemistry [4].

Since CO_2 absorption into KOH solution is generally governed by coupled mass transfer and reaction kinetics [4], an extensive understanding of interphase transfer phenomena is important. However, due to the microscale interphase mass transfer phenomena and complex hydrodynamics, experimental observation is often insufficient to capture these processes comprehensively. Therefore, Computational Fluid Dynamics (CFD) has become a valuable tool for modelling interphase mass transfer phenomena under the influence of bubble-column hydrodynamics [9]. Among various CFD approaches, the Euler–Euler multiphase method is particularly suitable for simulating gas–liquid systems containing large populations of dispersed bubbles. Within this framework, the phases are represented as interpenetrating continua, while momentum exchange between them can be described through interfacial-force closures such as drag, lift, turbulent dispersion, and wall lubrication. When combined with appropriate mass-transfer and reaction descriptions, the approach enables hydrodynamics and reactive absorption to be analysed within a unified spatial and temporal framework [10,11].

Previous CFD investigations have already addressed several important components of this coupled problem. Krauß and Rzehak developed an Euler–Euler/RANS framework for CO_2 chemisorption in aqueous NaOH in which hydrodynamics were coupled with reactive mass transfer, reaction kinetics, and an enhancement-factor formulation [12]. Liu et al. [8] subsequently evaluated four mass-transfer models and two enhancement-factor treatments within an Euler–Euler framework for CO_2–NaOH reactive absorption, demonstrating that the selection of these closures can substantially affect predictive performance. At a higher level of bubble-scale resolution, Taborda et al. [13] employed an Euler–Lagrange formulation with a dynamic Sherwood-number treatment to analyse CO_2 chemisorption in a cylindrical bubble column and compared the simulations with detailed experimental observations. Meanwhile, Li et al. [9] performed transient three-dimensional simulations to systematically assess alternative mass-transfer closures using spatially resolved gas-holdup and species-concentration data. Collectively, these studies demonstrate that Eulerian hydrodynamics, interfacial mass transfer, and chemical enhancement have already been incorporated into CFD descriptions of gas–liquid absorption; therefore, none of these individual modelling components constitutes the novelty of the present study.

Compared with these existing approaches, the present methodology serves a different modelling purpose. Studies such as Liu et al. [8] and Li et al. [9] primarily evaluated alternative mass-transfer or enhancement-factor closures, whereas the LES–Euler/Lagrange approach of Taborda et al. [13] provides a more detailed representation of individual bubble dynamics at greater modelling complexity. In contrast, the present study employs an engineering-scale Eulerian framework with

established interfacial-force, Higbie mass-transfer, and reaction-enhancement closures to examine transient semi-batch CO_2–KOH absorption. Its relative contribution is therefore not superior predictive accuracy over these previous approaches, but the experimentally constrained integration of reactor-scale breakthrough behaviour with spatially resolved hydrodynamic, mass-transfer, and reaction predictions within a single CO_2–KOH framework.

The contribution of the present study instead lies in the integrated application of these established modelling concepts to transient, semi-batch CO_2–KOH reactive absorption in a cylindrical bubble column and in using the experimentally measured CO_2 breakthrough response to interrogate the spatial coupling among reactor hydrodynamics, interfacial mass transfer, and reaction progression. Specifically, an Eulerian multiphase framework incorporating drag, lift, turbulent-dispersion, and wall-lubrication forces is coupled with Higbie penetration theory for liquid-side mass transfer and a reaction enhancement factor. Rather than comparing alternative closure models, the resulting framework is used to relate the transient outlet CO_2 response to spatially resolved predictions of superficial gas velocity, gas holdup, interfacial area, interphase mass-transfer coefficient, and reactive-species evolution. Accordingly, the objective of this study is to determine how local bubble-column hydrodynamics influence reactive CO_2 uptake in aqueous KOH and to establish a mechanistically interpretable CFD framework that can support subsequent analysis and optimization of semi-batch CO_2 absorption systems.

2. Research Methodology

Experiments on the chemisorption of CO_2 in KOH solution were established in a laboratory–scale bubble column, as demonstrated in Fig. 1 (a). The column had an internal diameter of 0.14 m and the liquid height used as the simulation domain was set to 0.7 m. A gas distributor with a diameter of 0.08 m was installed located at the underside of the bubble column to inject the gas phase.

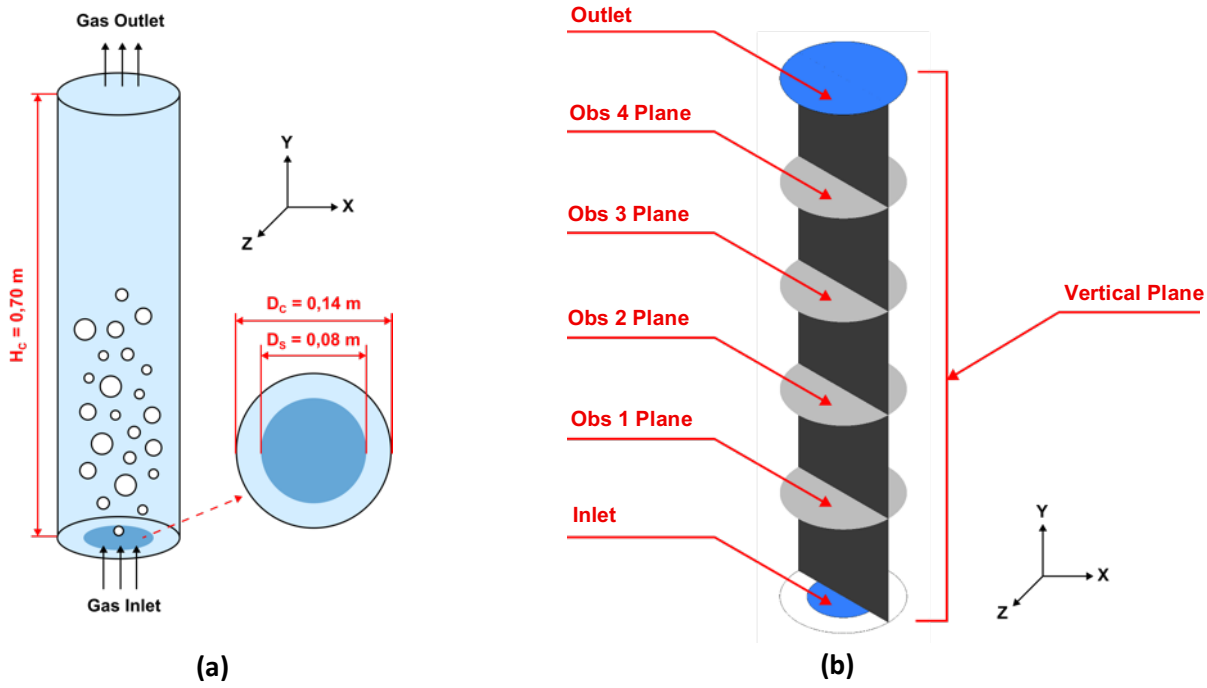

Fig. 1. (a) Bubble Column Schematic Diagram for Domain Simulation. (b) Observation Plane

Furthermore, the observation planes for the analysis are illustrated in Fig. 1 (b). The simulation domain was divided into two categories, axial and radial plane. The axial plane was used to observe the vertical hydrodynamic behaviour along the bubble column, extending from inlet at the bottom to the outlet at the topside of the reactor. Meanwhile, the radial plane was utilized to evaluate the hydrodynamic characteristic from the centre region toward the near–wall area at different column heights. The detailed coordinates of each observation plane are summarized in Table 1 below.

Table 1
Plane Observation Detail

Plane Name	Plane Coordinate	Distance (m)
Inlet	XZ	Y = 0.00
Obs 1	XZ	Y = 0.14
Obs 2	XZ	Y = 0.28
Obs 3	XZ	Y = 0.42
Obs 4	XZ	Y = 0.56
Outlet	XZ	Y = 0.70
Vertical	XY	Z = 0.00

In the present work, KOH solution with a concentration of 0.15 mol/L was utilized as the liquid phase and treated as a constant liquid within the column, so that this system became semi-batch system. The gas volumetric flow was 3.0 L/min with initial gas velocity values of 0.00315 m/s, respectively. Direct contact among the CO_2 bubbles and the KOH solution within the column facilitated the interphase mass transfer process and subsequent chemisorption reaction. At the top of the column, a CO_2 gas detector was installed to measure the concentration of unabsorbed CO_2. During the chemisorption process the operating temperature and pressure was ambient, respectively. Therefore, the physical properties under the operating conditions were elaborated on Table 2 below:

Table 2
Physical Properties under the Operating Conditions

Parameters	Values	Units	Annotation	References
Density of Gas, (ρ_G)	1.722	kg.m^{-3}	Estimated	FLUENT Database
Viscosity of Gas, (μ_G)	1.37×10^{-5}	Pa.s^{-1}	Estimated	FLUENT Database
Density of Liquid, (ρ_L)	1002.68	kg.m^{-3}	Calculated	[14]
Viscosity of Liquid, (μ_L)	8.70×10^{-5}	Pa.s^{-1}	Calculated	[14]
Molecular Weight of Liquid, (M_L)	18.105	kg.kmol^{-1}	Calculated	-
Surface Tension, (σ)	0.07294	N.m^{-1}	Estimated	[9]
CO_2 Diffusivity Coefficient, $\left(D_L^{CO_2}\right)$	1.4663×10^{-9}	m^2.s^{-1}	Estimated	[9]
OH^- Diffusivity Coefficient $(D_L^{OH^-})$	5.27×10^{-9}	m^2.s^{-1}	Estimated	[15]
Henry's Constant, $(\mathcal{H})$	2.914×10^6	Pa.m^3.kmol^{-1}	Calculated	[21,22]
Universal Gas Constant, (R)	8.314	J.mol^{-1}.K^{-1}	Estimated	-

This work performed a three–dimensional simulation study of hydrodynamic in the bubble column using CFD solver of ANSYS Fluent under time–dependent approaches. The governing equations were derived through the finite volume method. Pressure–velocity coupling was resolved by the SIMPLE phase–coupled procedure. The gradients were computed utilizing the least squares cell–based method. A time step size of 0.1 s with number of time steps of 6,000 was employed during simulation. Convergence was assumed for each time steps when the residuals of all governing equations fell below 0.001 and a maximum 50 iteration per time step was adopted.

The final transient simulations employed Grid 3 with 9,840 computational cells, a time step of 0.1 s, and 6.000-time steps. The calculations were performed using ANSYS Fluent on a Lenovo ThinkPad X1 Carbon Gen 9 equipped with an Intel Core i7-1185G7 processor (4 physical cores, 8 logical processors) and 16 GB RAM. For this relatively compact computational domain, a complete 600 s transient simulation required several hours of computation, with the computational demand depending primarily on the number of iterations required for convergence at each time step.

3. Mathematical Model

3.1 Eulerian Multiphase Model

In the present study, CFD methods were conducted using the Eulerian multiphase model. This approach treats the liquid and gas phases as interpenetrating continua within a shared computational domain. Furthermore, this model provides a computationally efficient framework for simulating gas-liquid systems with many dispersed bubbles, while adequately capturing phase interactions through average mass, momentum, and species balance equations [9].

Mass Balance:

$$\frac{\partial \alpha_q \rho_q}{\partial t} + \nabla \cdot \left(\alpha_q \rho_q \vec{u}_q\right) = \dot{m}_q \tag{1}$$

Momentum Balance:

$$\frac{\partial \alpha_q \rho_q \vec{u}_q}{\partial t} + \nabla \cdot \left(\alpha_q \rho_q \vec{u}_q \vec{u}_q\right) = \alpha_q \nabla p + \nabla \cdot \left\{\alpha_q \mu_q \left[\nabla \vec{u}_q + \left(\nabla \vec{u}_q\right)^T - \frac{2}{3}\left(\nabla \vec{u}_q\right)\bar{\bar{I}}\right] - \frac{2}{3}\alpha_q \rho_q k^q \bar{\bar{I}}\right\} \alpha_q \rho_q \vec{g} + \vec{M}_q \tag{2}$$

Species Balance:

$$\frac{\partial \alpha_q \rho_q X_q^i}{\partial t} + \nabla \cdot \left(\alpha_q \rho_q \vec{u}_q X_q^i\right) = \nabla \left[\left(\mathrm{D}_{\mathrm{q}}^{\mathrm{i,m}} + \frac{\mu_q^t}{\rho_q Sc_t}\right) \alpha_q \rho_q \nabla X_q^i\right] + \dot{m}_q^i, \text{ where } \sum_{q=1}^{n} \alpha_q = 1 \tag{3}$$

The subscript q denotes the phase index, where G and L represent gas and liquid phases, respectively. The phase volume fraction satisfies the conservation constraint:

$$\sum_{q=1}^{n} \alpha_q = 1 \tag{4}$$

$\vec{M}_q$ represents the total interphase momentum exchange due to interfacial forces within the gas and liquid phases.

In this work, drag, lift, turbulent dispersion, and wall lubrication were examined. Based on repeated visual observations of bubble formation during the absorption experiments, an average bubble diameter of approximately 2.9 mm was determined throughout the simulation. The total of interphase momentum exchange could be written as:

$$\vec{M}_{L\to G} = -\vec{M}_{G\to L} = \vec{F}_{D,(L\to G)} + \vec{F}_{L,(L\to G)} + \vec{F}_{TD,(L\to G)} + \vec{F}_{WL,(L\to G)} \tag{5}$$

Drag force is the dominant force governing interphase momentum transfer and strongly influences bubble rise velocity and gas holdup distribution [6,23]. In this study, the drag coefficient was calculated using the correlation proposed by Tomiyama [19]. Drag force is formulated as follows:

$$\vec{F}_{D,(L\to G)} = -\frac{3}{4}\alpha_G \rho_L \frac{C_D}{d_B}|\vec{u}_G - \vec{u}_L| \; ; C_D = \max\left\{\min\left[\frac{24}{Re_B}\left(1 + 0{,}15Re_B^{0{,}687}\right); \frac{72}{Re_B}\right]; \frac{8}{3}\frac{E\ddot{o}}{E\ddot{o}+4}\right\} \quad (6)$$

Lift force arises from liquid velocity gradients and acts perpendicular to the relative bubble motion, influencing the radial redistribution of bubbles within the column. Tomiyama lift force model [20] was used in the present work and is formulated below.

$$\vec{F}_{L,(L\to G)} = -C_L \alpha_G \rho_L (\vec{u}_G - \vec{u}_L)(\nabla \times \vec{u}_L) \quad (7)$$

where (C_L) is the lift force coefficient.

The turbulent dispersion force accounts for turbulent fluctuations in the continuous phase and promotes the redistribution of bubbles from regions of high gas concentration toward regions of lower gas concentration. Burn et al., 2004 [21] expressed this using Favre-averaging as:

$$\vec{F}_{TD,(L\to G)} = -\frac{3}{4} C_{TD} \alpha_L (1-\alpha_L) \frac{C_D}{d_B}|\vec{u}_G - \vec{u}_L| \frac{\mu_L^{turb}}{\sigma_{TD}}\left(\frac{\nabla \alpha_L}{\alpha_L} - \frac{\nabla \alpha_G}{\alpha_G}\right) \quad (8)$$

Wall lubrication force acts in the near-wall region and counterbalances excessive bubble accumulation adjacent to the column wall, thereby improving the prediction of radial gas holdup profiles. Frank et al., 2005 [22] formulated the correlation for wall lubrication force as follows:

$$\vec{F}_{WL,(L\to G)} = -\frac{2}{d_B} C_{WL} \rho_L \alpha_G \left|(\vec{u}_G - \vec{u}_L)_{\parallel}\right|^2 \vec{y} \; ; C_{WL} = C_W(E\ddot{o}) \cdot \max\left\{0 \; ; \frac{1}{y_W C_{WD}} \cdot \left[1 - \frac{y_W}{C_W d_B}\right]\left[\frac{y_W}{C_W d_B}\right]^{1-p}\right\} \quad (9)$$

where $(\vec{u}_G - \vec{u}_L)_{\parallel}$ denotes the tangential relative velocity, $\vec{y}$ is the unit normal to the wall, where C_{WC} and C_{WD} denote the cut-off and damping coefficient used in the wall lubrication coefficient.

Bubble deformation effects were implicitly accounted for through the Eötvös number incorporated in the Tomiyama drag and lift correlations [24,25]. Besagni et al. [7] categorized turbulent dispersion and wall lubrication forces as a non-drag-force (NDF). Furthermore, Ziegenhein et al. [23] demonstrated that the deployment of these NDFs can significantly improve gas holdup prediction. These interfacial forces consequently influence the prediction of bubble dynamics and gas holdup distribution, thereby playing a crucial role in bubble column reactive absorption systems.

3.2 Interphase Mass Transfer and Reaction Model

The volumetric interphase mass exchange rate of species *i* into phase *q* $\left(\dot{m}_q^i\right)$ in Eq. (3) arises from interphase mass transfer. CO_2 is considered as the only transferred species, and its dissolution into the liquid phase is assumed to occur under saturation conditions, resulting in accumulation of dissolved CO_2 concentration in the liquid phase. Michelson et al. [24] integrated the accumulated CO_2 concentration through the following expression:

$$\dot{m}_L^{CO_2} = Ek_L a\left(C^*_{CO_2} - C_t\right) \; ; a = \frac{6\alpha_G}{d_B} \quad (10)$$

here, a is the interfacial area, α_G is the gas holdup, d_B expresses bubble diameter, $C^*_{CO_2}$ is the saturation concentration of dissolved CO_2, C_t represents the bulk dissolved CO_2 concentration in the liquid phase in a certain time. $C^*_{CO_2}$ is estimated as follows:

$$C^*_{CO_2} = \frac{RT}{\mathcal{H}(T)}\frac{\rho_L}{M_L} \quad (11)$$

where R represents the universal gas constant, $\mathcal{H}(T)$ denotes the Henry's constant of CO_2 at temperature T, ρ_L exhibits the solution density, and M_L marks the molecular weight of the solution. Versteeg & Swaaij, (1980) [16] investigated the dissolution of gases in water at 25 °C and atmospheric pressure and proposed generalized correlations for Henry's constant, later modified by Sander [17] as follows:

$$\mathcal{H}(T) = \mathcal{H}(T_0) \cdot \exp\left[\frac{\Delta H_{Sol}}{R}\left(\frac{1}{T} - \frac{1}{T_0}\right)\right] \quad (12)$$

For this study, the Higbie penetration theory [25] was employed to calculate the value of interphase mass transfer coefficients. This correlation was used because many industrial gas-liquid processes operate under insufficient contact times to establish steady-state diffusion films. Consequently, the assumptions of classical film theory become less appropriate than those of penetration theory [24].

$$k_L = 2\sqrt{\frac{D_L^{CO_2}}{\pi}}\left(\frac{\varepsilon\rho_L}{\mu}\right)^{\frac{1}{4}} \tag{13}$$

where $D_L^{CO_2}$ expresses the CO_2 diffusivity coefficient, t_c denotes contact time. In addition, this correlation is particularly suitable when the bubble diameter exceeds 2.5 mm and in the high turbulence conditions [9,30].

The enhancement factor represents the ratio between liquid-side mass transfer flux in the presence of chemical reaction with purely physical absorption conditions for an identical concentration driving force [16,18]. In the present study, a penetration-theory-based enhancement factor correlation was employed [28].

$$E = -\frac{Ha^2}{2(E_i-1)} + \sqrt{\frac{Ha^4}{4(E_i-1)^2} + E_i\frac{Ha^2}{(E_i-1)} + 1}\ ; Ha = \frac{\sqrt{k_R D_L^{CO_2} C_{OH^-}}}{k_L} \tag{14}$$

where Ha denotes Hatta number, expressing the relative magnitude of reaction kinetics to molecular diffusion within the liquid film. According to Krauβ and Rzehak [27], Eq. (14) is appropriately applied to both penetration and renewal theory. Hence, the penetration-based enhancement factor was adopted to account for the acceleration of CO_2 absorption resulting from chemical reactions. The individual Higbie and enhancement-factor expressions are established closures; their role in the present framework is to provide a physically interpretable coupling between the locally resolved Eulerian hydrodynamics and reactive liquid-side CO_2 transfer rather than to constitute newly developed sub-models.

3.3 Standard k-ε Turbulence Model

Turbulence effects in the continuous phase were modelled using the standard k-ε turbulence model. The model is formulated as follows:

$$\frac{\partial \alpha_L\rho_L k}{\partial t} + \nabla\cdot(\alpha_L\rho_L\vec{u}_L k) = \nabla\cdot\left[\alpha_L\left(\mu_L^m + \frac{\mu_L^t}{\sigma_k}\right)\nabla k\right] + \alpha_L G_k - \alpha_L\rho_L\varepsilon + S^k \tag{15}$$

$$\frac{\partial \alpha_L\rho_L \varepsilon}{\partial t} + \nabla\cdot(\alpha_L\rho_L\vec{u}_L \varepsilon) = \nabla\cdot\left[\alpha_L\left(\mu_L^m + \frac{\mu_L^t}{\sigma_k}\right)\nabla\varepsilon\right] + C_{\varepsilon_1}\alpha_L\frac{\varepsilon}{k}G_k - C_{\varepsilon_2}\alpha_L\rho_L\frac{\varepsilon^2}{k} + S^\varepsilon \tag{16}$$

the constants are specified as follows: $C_\mu = 0.09$; $C_1 = 1.44$; $C_2 = 1.92$; $\sigma_k = 1.0$; and $\sigma_\varepsilon = 1.3$.

In addition, the standard k-ε model was adopted owing to its numerical stability, computational efficiency, and extensive application in gas-liquid bubble column simulations. The resulting turbulence field influences bubble dispersion, gas holdup distribution, and consequently the interphase mass transfer processes within the reactor.

3.4 Model Assumptions, Limitations, and Range of Applicability

The present CFD framework involves several simplifying assumptions that should be considered when interpreting the results. The Eulerian–Eulerian formulation treats the gas and liquid phases as

interpenetrating continua and therefore describes phase-averaged rather than individual-bubble behaviour. In addition, a constant bubble diameter of 2.9 mm was imposed throughout the simulation. Consequently, bubble coalescence, breakup, polydispersity, and bubble-history effects were not explicitly resolved. The predicted gas distribution, gas holdup, and interfacial area also depend on the selected drag, lift, turbulent-dispersion, and wall-lubrication closures and on the standard k−ε representation of the continuous-phase turbulence. These modelling choices are consistent with the framework described in Sections 3.1 and 3.3 but may introduce uncertainty when substantial bubble-size evolution or more complex flow structures occur.

For interphase transport, the liquid-side mass-transfer coefficient was calculated using Higbie penetration theory, which represents mass transfer through transient exposure and renewal of liquid elements at the gas–liquid interface. The resulting coefficient therefore depends on the suitability of the assumed interfacial contact-time representation for the actual bubble dynamics. Chemical enhancement was incorporated through a penetration-theory-based enhancement factor expressed in terms of the Hatta number. This approach represents reaction-accelerated CO_2 transfer through an effective closure rather than explicitly resolving the complete microscale reaction–diffusion field; consequently, its predictive accuracy depends on the validity of the underlying kinetic, diffusional, and reaction-regime assumptions for the investigated CO_2–KOH system.

Accordingly, the present framework should be interpreted as an engineering-scale model for the investigated semi-batch bubbly-flow system rather than as a universally validated description of CO_2 absorption in bubble columns. Quantitative validation is presently limited to the transient CO_2 breakthrough response obtained for a 0.14 m diameter column, a liquid height of 0.70 m, 0.15 mol/L KOH, and a gas flow rate of 3.0 L/min under ambient conditions. Application to substantially different column dimensions, gas velocities, bubble-size distributions, flow regimes, absorbent concentrations, or reactor configurations would require reassessment of the relevant closure relations and additional experimental validation. The Eulerian formulation provides a computationally tractable engineering-scale framework that may support parametric evaluation and reactor-design studies without resolving individual bubble trajectories. However, extension to industrial-scale columns should not be regarded as a direct geometric scale-up, because changes in gas throughput, bubble-size distribution, flow regime, turbulence, and column geometry may require different closure formulations and independent validation.

4. Result and Discussion

4.1 Grid Independency Study

A grid independence study was performed to verify that the simulation results were independent from grid resolution. On the other perspective, the study was intended to optimize computational cost in the ANSYS Fluent CFD Solver. Since the objective of this section was solely to evaluate mesh sensitivity, a constant mass transfer coefficient was adopted to isolate the effect of grid resolution. Four grids were adopted as presented on the Table 3 below.

Table 3
Grid Independency Study Result

No	Grid	Gas Velocity Outlet (m/s)	Relative Error with Previous Grid	CO_2 Mass Fraction Outlet in Gas Phase	Relative Error with Previous Grid
1.	7,424	0.07805	-	0.52418	-
2.	8,564	0.07662	1.83%	0.54325	1.75%
3.	9,840	0.07753	1.19%	0.54948	1.09%
4.	12,918	0.07696	0.74%	0.55025	0.14%

Two parameters, gas velocity and CO_2 mass fraction in gas phase, were observed in the outlet stream with 0.03157 m/s as an initial gas velocity. Table 3 shows that the predicted outlet gas velocity and CO_2 mass fraction varied noticeably between Grid 1 and Grid 2 with relative error of 1.83% and 1.75%, respectively. Further refinement from Grid 2 to Grid 3 resulted in smaller relative differences of 1.19% and 1.09%. Ultimately, only marginal changes were observed between Grid 3 and Grid 4. Therefore, considering that refinement from Grid 3 (9,840 cells) to Grid 4 (12,918 cells) changed the outlet gas velocity and CO_2 mass fraction by only 0.74% and 0.14%, respectively, Grid 3 was selected as the final mesh to balance numerical resolution and computational demand.

4.2 Simulation Validation

Figure 2(a) illustrates the transient reactive absorption behaviour during the 10 min process. At the beginning of the experiment, the fresh KOH solution provides a high absorption capacity, resulting in a negligible normalized CO_2 concentration at the reactor outlet. As absorption proceeds and the available alkalinity is progressively consumed, the outlet CO_2 concentration increases, reflecting a reduction in the overall absorption driving force [29]. Consequently, an S-shaped breakthrough profile is observed, representing the gradual progression from high initial CO_2 uptake toward absorbent saturation.

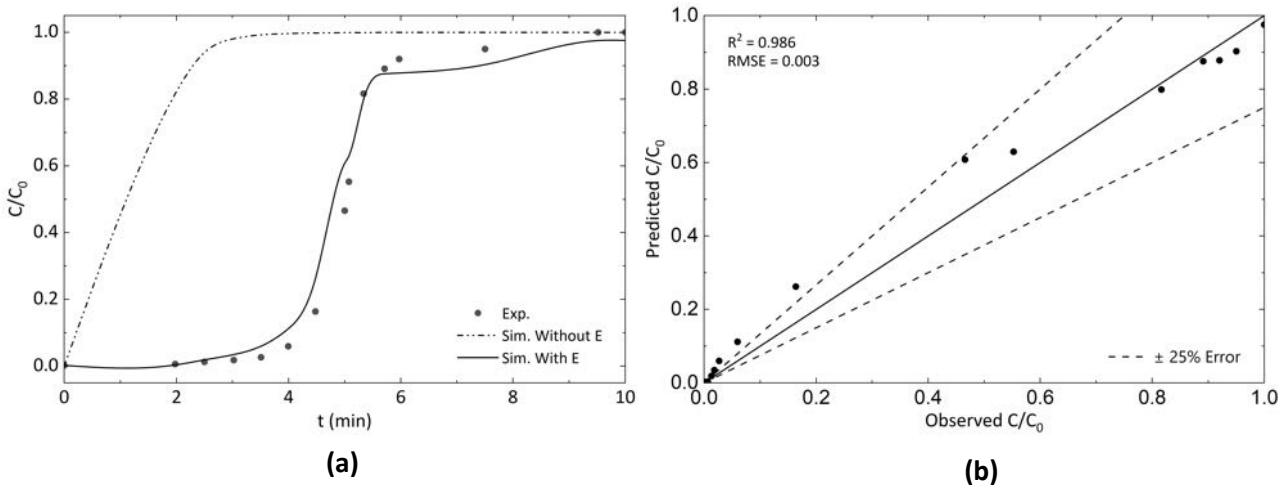

Fig. 2. Comparison between CFD simulations and experimental measurements of normalized CO_2 outlet concentration: (a) transient breakthrough profiles with and without the enhancement factor and (b) observed versus predicted values for the model incorporating the enhancement factor

Model validation was performed by comparing the experimentally measured normalized outlet CO2 concentration with the CFD predictions, as shown in Fig. 2(a). The corresponding observed-versus-predicted comparison for the model incorporating the enhancement factor is presented in

Fig. 2(b). Statistical analysis demonstrates close agreement between the experimental and simulated breakthrough responses, with an R^2 of 0.986 and an RMSE of 0.003. These results demonstrate that the integrated CFD framework reproduces the experimentally observed transient outlet CO_2 behaviour under the investigated operating condition.

During approximately the first 3 min of operation, only a small fraction of CO_2 is detected at the reactor outlet, consistent with the high initial absorption capacity of the alkaline solution. The high OH^- concentration promotes rapid consumption of dissolved CO_2 and thereby sustains CO_2uptake [30]. After approximately 3 min, the normalized outlet concentration increases progressively and approaches $C/C_0 = 1.0$ after approximately 7 min, indicating progressive exhaustion of the available absorption capacity. The validated breakthrough response was subsequently used as the experimental basis for interpreting the CFD-derived hydrodynamic, mass-transfer, and reaction behaviour at 3 min, corresponding to a period of high reactive absorption activity.

It should be emphasized that the quantitative validation performed in the present study is restricted to the transient normalized outlet CO_2 concentration. Accordingly, the agreement shown in Fig. 2 validates the ability of the integrated framework to reproduce the experimentally observed breakthrough behaviour at the investigated operating condition. The spatially resolved quantities discussed in the following sections—including superficial gas velocity, gas holdup, interfacial area, interphase mass-transfer coefficient, and species distributions—were not independently validated against spatial experimental measurements and should therefore be interpreted as model predictions rather than experimentally validated fields. This distinction defines the scope of the validation used throughout the subsequent analysis.

4.3 Bubble Column Regime and Hydrodynamic Analysis

The hydrodynamic characteristics of a bubble column strongly influence its reactive absorption performance. Among these characteristics, superficial gas velocity is an important parameter governing the prevailing gas–liquid flow regime. Bubble-column operation is commonly categorized into homogeneous, transition, and heterogeneous regimes. The homogeneous or bubbly-flow regime is generally favourable for gas–liquid absorption because it is associated with relatively uniform gas dispersion, stable hydrodynamic behaviour, and substantial gas–liquid interfacial area [31].

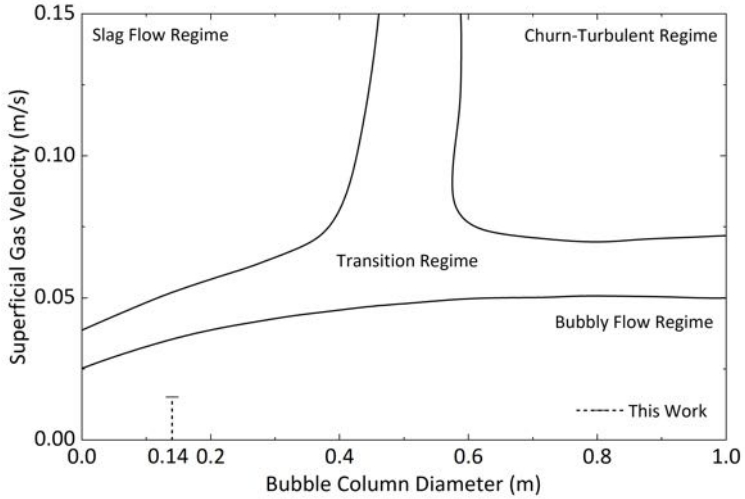

Fig. 3. Approximate bubble-column flow-regime estimation adapted from Deckwer et al. [32]

Deckwer et al. [32] developed a geometry-based flow-regime map relating column diameter to superficial gas velocity, as shown in Fig. 3. According to this map, relatively low superficial gas velocities are associated with homogeneous bubbly-flow conditions. In the present study, the column diameter was 0.14 m and the inlet superficial gas velocity was 0.00315 m/s, while the maximum superficial gas velocity predicted by the CFD simulation was approximately 0.0151 m/s. These operating values lie within the bubbly-flow region of the regime map, supporting the classification of the investigated reactor condition as homogeneous bubbly flow.

The predicted hydrodynamic state is also qualitatively consistent with previous bubble-column observations. Krishna and van Baten reported that homogeneous bubbly flow is generally associated with relatively dispersed bubble populations, with bubble diameters of approximately 1–7 mm reported for air–water systems. The constant bubble diameter of 2.9 mm adopted in the present model therefore lies within a characteristic size range associated with dispersed bubbly operation. Nevertheless, quantitative comparison of gas holdup among different studies should be made cautiously because gas holdup depends strongly on column geometry, gas-distributor configuration, liquid properties, bubble-size distribution, and superficial gas velocity.

The predicted superficial gas velocity distribution is presented in Fig. 4. As shown in Fig. 4(a), the highest local superficial gas velocities occur near the gas distributor, where the injected gas retains relatively high momentum. Moving upward through the column, the gas-velocity distribution becomes progressively more uniform as the inlet momentum dissipates through gas–liquid interactions.

Bubble redistribution is influenced by the interfacial-force closures incorporated in the model. Tomiyama et al. [19] reported that bubbles below a critical diameter of approximately 5.4 mm under atmospheric conditions generally exhibit a positive lift coefficient and tend to migrate toward the column wall, whereas larger bubbles may preferentially migrate toward the column centre. Given the 2.9 mm constant bubble diameter adopted in the present simulation, the predicted tendency toward increased bubble presence in intermediate-to-wall regions is qualitatively consistent with this lift-force behaviour. The resulting distribution reflects the combined effects of lift, wall lubrication, and turbulent dispersion rather than the action of any single interfacial force.

Figure 4(b) shows the radial profiles of superficial gas velocity at different axial locations. Relatively high gas velocities are predicted primarily between $r/R = -0.25$ and -0.75, whereas lower values occur around the column centre. A secondary increase is observed within the positive intermediate radial region. Immediately adjacent to the wall, the predicted gas velocity decreases, consistent with the combined influence of wall lubrication and liquid–wall interactions. Turbulent dispersion additionally acts to redistribute bubbles from locally concentrated regions toward regions of lower gas concentration [21]. With increasing axial height, the radial profiles become progressively flatter, indicating dissipation of the inlet momentum and a more spatially distributed gas flow.

Gas holdup provides an additional measure of the predicted gas-phase distribution within the column. Figure 5(a) shows the axial and radial gas-holdup fields. The highest local gas holdup occurs near the gas distributor, followed by a progressively more uniform distribution along the column height. This simulated behaviour is consistent with the homogeneous bubbly-flow interpretation derived from the regime map, although the spatial gas-holdup field itself was not independently validated experimentally.

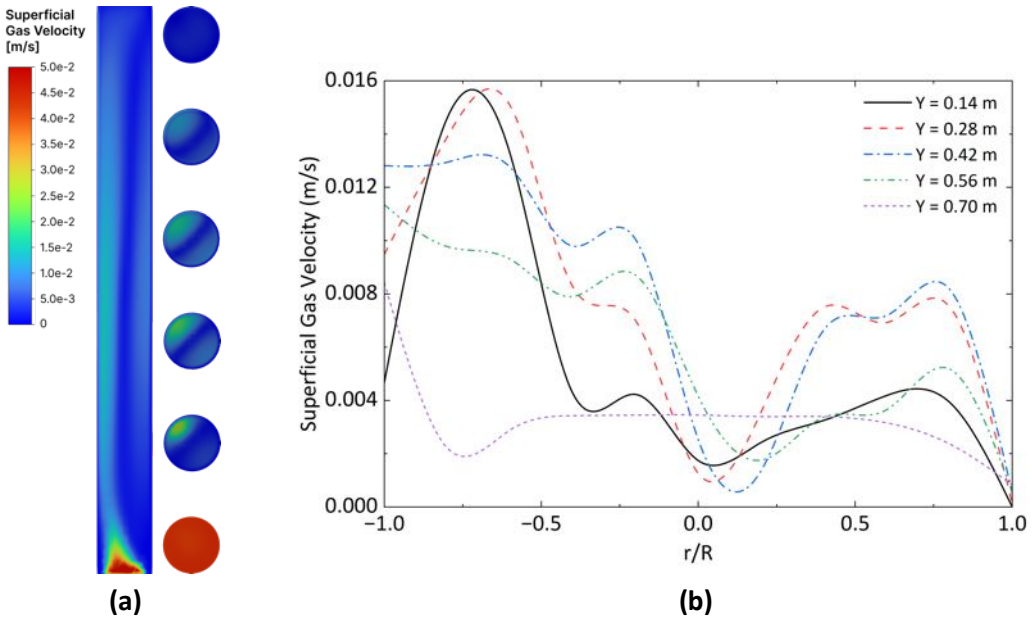

Fig. 4. Spatial distributions of superficial gas velocity: (a) axial and cross-sectional contours and (b) radial profiles at different axial positions

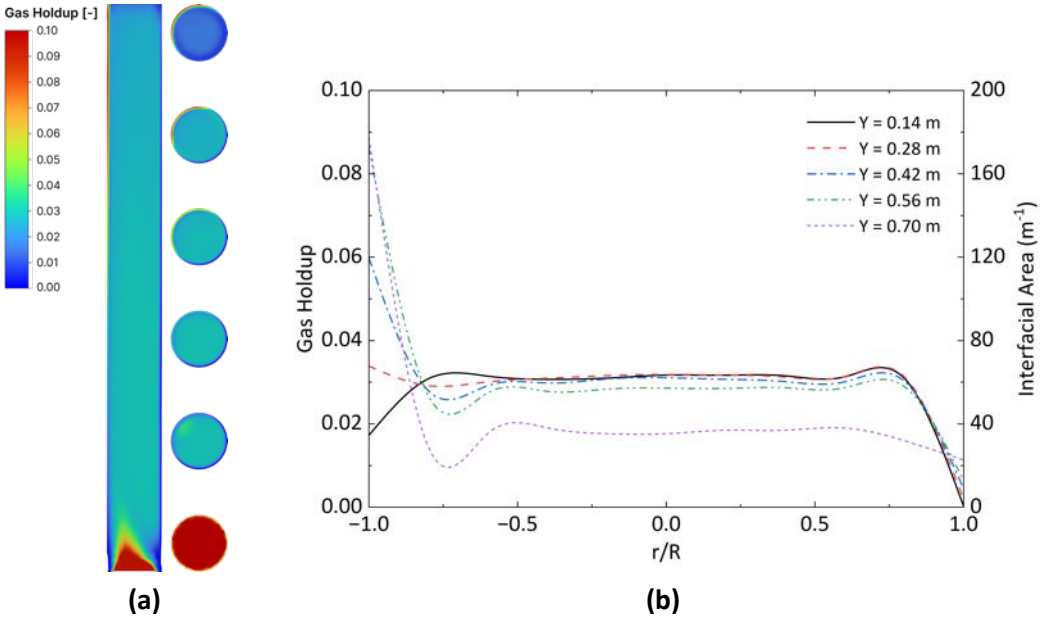

Fig. 5. Spatial Distribution Profiles of Interphase Gas Holdup, **(a)** Axial and Cross-Sectional Contour of Gas Holdup along the Bubble Column Height, **(b)** Radial Profiles of Interphase Gas Holdup and Interfacial Area at Five Axial Positions

Gas-holdup predictions are sensitive to the selected interfacial-force closures, particularly non-drag forces such as lift, turbulent dispersion, and wall lubrication. Turbulent dispersion promotes redistribution of bubbles from regions of high gas concentration toward regions of lower concentration, thereby limiting localized gas accumulation [7]. Despite local radial velocity gradients, the simulation does not predict severe gas channelling or extensive gas-rich regions. The volume-averaged gas holdup was approximately 0.089. Rather than serving as an isolated performance metric, this value represents the fraction of reactor volume occupied by the gas phase under the

specific geometry and relatively low superficial gas velocity investigated here. Accordingly, it should be interpreted within the present operating envelope rather than as a universal reference value for CO_2 absorption in bubble columns [33].

Figure 5(b) demonstrates the relationship between the predicted gas holdup and gas–liquid interfacial area at different axial positions. Both parameters are relatively uniform throughout much of the column but decrease near the upper liquid region as bubbles approach the disengagement zone. The average predicted gas–liquid interfacial area was 177.8 m^{-1}. Because a constant bubble diameter of 2.9 mm was imposed in the Eulerian formulation, the interfacial area is directly related to the predicted gas holdup through Eq. (10). Consequently, the interfacial-area field should not be regarded as an independent hydrodynamic prediction. Instead, it translates the predicted gas-phase distribution into the gas–liquid surface area available for interphase transfer: regions of higher gas holdup correspond to greater available interfacial area for CO_2 transport.

4.4 Interphase Mass Transfer Coefficient Behaviour

The Higbie penetration model was employed to calculate the liquid-side interphase mass-transfer coefficient. According to penetration theory, mass transfer is governed by transient exposure and renewal of liquid elements at the gas–liquid interface. Hydrodynamic conditions that promote more frequent interfacial renewal can therefore increase the predicted mass-transfer coefficient.

As shown in Fig. 6(a), relatively high interphase mass-transfer coefficients are predicted between Y=0.28 and 0.42 m, particularly around r/R=−0.25. This region corresponds to areas of relatively high superficial gas velocity identified in Fig. 4. Increased local gas motion can promote liquid circulation and interface renewal, thereby reducing effective interfacial contact time within the Higbie formulation and increasing the predicted mass-transfer coefficient. Shen et al. [34] similarly reported that bubble clustering and swarm motion can intensify local liquid mixing through wake interactions, thereby influencing gas–liquid mass transfer. In addition, rapid consumption of dissolved CO_2 by OH^- maintains a low bulk dissolved- CO_2 concentration and consequently sustains the interfacial concentration driving force [35].

Figure 6(b) shows the radial profiles of the predicted interphase mass-transfer coefficient. Near the distributor, moderate values are obtained, followed by an increase to the highest profile at approximately Y = 0.28 m. This axial location also exhibits relatively high superficial gas velocities, suggesting stronger local gas–liquid interactions within the model. Farther upward, the mass-transfer coefficient decreases progressively as inlet momentum dissipates and the predicted hydrodynamic field becomes more uniform. A similar qualitative dependence of gas–liquid transfer on superficial gas velocity has been reported by Shen et al. [34],

The spatially averaged interphase mass-transfer coefficient was approximately 0.0065 m/s. This value should be interpreted specifically as a Higbie-model prediction under the present hydrodynamic and physical-property conditions, rather than as a universally applicable liquid-side mass-transfer coefficient. Previous CFD investigations have shown that predicted mass transfer may vary substantially with the selected closure formulation. Chen and Brooks [33], for example, compared penetration-, surface-renewal-, and analogy-based mass-transfer descriptions against bubble-column experiments, whereas Li et al. [9] demonstrated the sensitivity of spatial mass-transfer predictions to the selected closure. Accordingly, the primary significance of the present result lies in its spatial variation and its mechanistic relationship with the predicted hydrodynamic field, rather than in the absolute value alone.

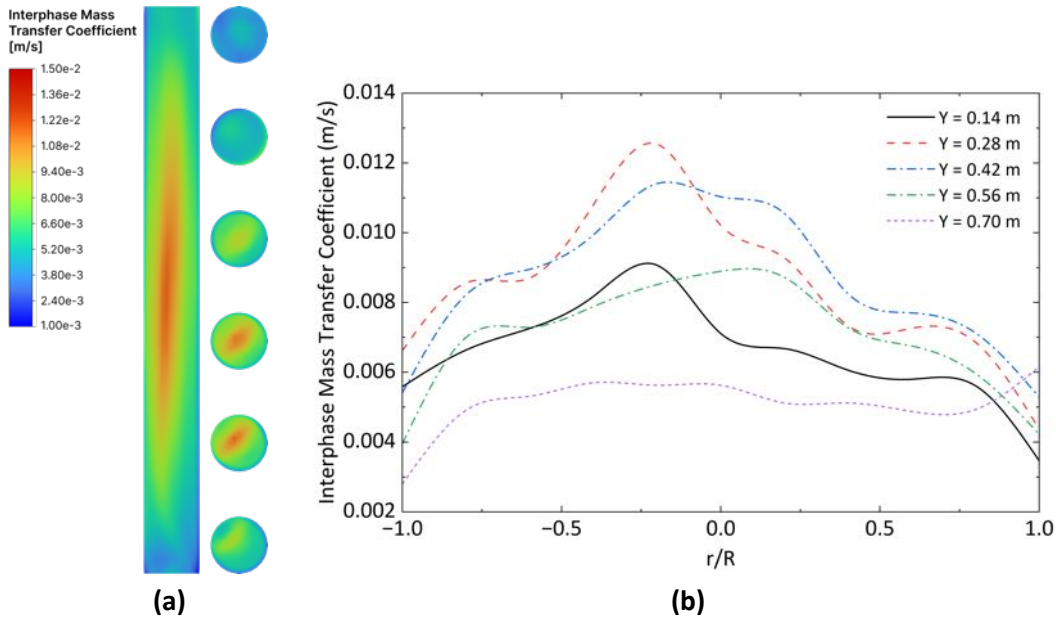

Fig. 6. Spatial distributions of the interphase mass-transfer coefficient: (a) axial and cross-sectional contours and (b) radial profiles at five axial positions

4.5 Reactive Absorption Behaviour

CO_2 introduced into the column as dispersed gas bubbles undergoes simultaneous interphase transfer, dissolution, and liquid-phase reaction. Figure 2(a) demonstrates that the simulation incorporating the reaction enhancement factor reproduces the experimentally observed breakthrough response substantially better than the corresponding simulation without chemical enhancement. The simulation without enhancement represents the limiting case in which reactive acceleration of liquid-side transfer is neglected. Under this condition, accumulation of dissolved CO_2 progressively reduces the concentration driving force and results in earlier breakthrough.

By contrast, when the enhancement factor is included, rapid consumption of dissolved CO_2 by hydroxide ions increases the effective reactive-transfer flux and sustains the concentration driving force for a longer period. The enhancement factor should not be interpreted as an additional hydrodynamic mass-transfer coefficient. Rather, it represents the acceleration of interfacial CO_2 transfer resulting from the coupled liquid-phase chemical reaction, whereas the Higbie formulation independently determines the liquid-side mass-transfer coefficient. These two components therefore play distinct roles within the coupled transport framework.

The improvement in breakthrough prediction obtained by including chemical enhancement is consistent with previous reactive-absorption modelling. Liu et al. [7] demonstrated for CO_2 absorption into aqueous NaOH that accounting explicitly for a variable enhancement factor produced more accurate predictions than assuming an enhancement factor of unity. Similarly, Krauß and Rzehak [12], [27] showed that the description of carbonate–bicarbonate chemistry and reaction-enhanced mass transfer is critical for representing CO_2 absorption in alkaline solutions. The present comparison between simulations with and without enhancement therefore supports the importance of chemical-reaction coupling in reproducing the transient CO_2 uptake observed experimentally.

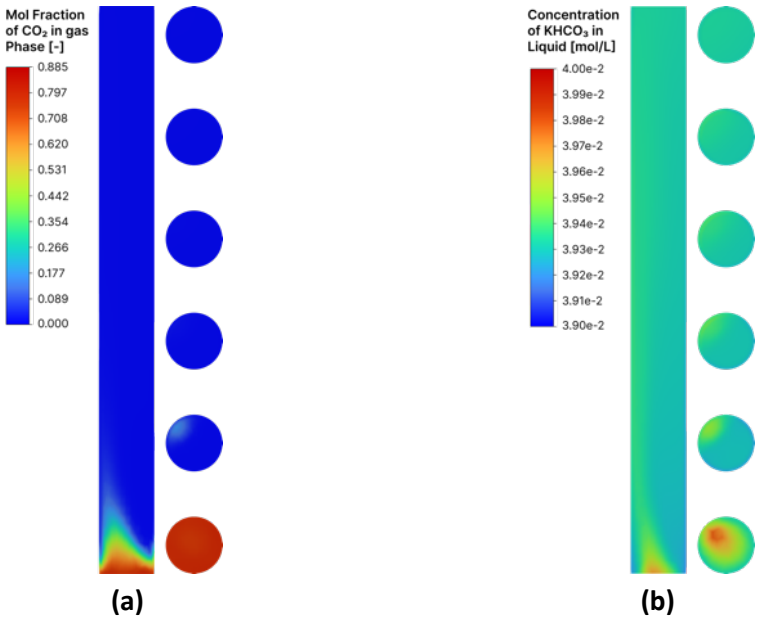

Fig. 7. Predicted spatial distributions of species during reactive absorption: (a) CO_2 mole fraction in the gas phase and (b) aqueous-phase $KHCO_3$ concentration prior to product recovery and thermal treatment

The predicted species distributions are shown in Fig. 7. Near the gas distributor, the CO_2 mole fraction in the gas phase remains relatively high because the entering bubbles have undergone limited absorption. A pronounced decrease is subsequently predicted within the lower axial region, before approximately Y=0.14 m, indicating substantial CO_2 transfer from the gas phase. Beyond this region, the predicted gas-phase CO_2 fraction remains comparatively low through much of the column, consistent with continued reactive uptake by the KOH solution. These spatial trends should be regarded as mechanistic predictions of the validated framework rather than independently validated concentration fields.

Krauß and Rzehak [27] described a series of reversible pathways governing CO_2 absorption in alkaline solutions, as summarized in Table 4. Initially, dissolved CO_2 reacts rapidly with hydroxide ions through the hydroxide pathway to form bicarbonate-containing species. A smaller contribution may occur through hydration and associated acid–base equilibria, while the hydroxide pathway dominates under strongly alkaline conditions.

Table 4
Reaction Pathways during CO_2 Reactive Absorption

Reaction	Pathway
$CO_{2\,(aq)} + OH^-_{(aq)} \rightleftharpoons HCO^-_{3\,(aq)}$	Hydroxide
$CO_{2\,(aq)} + H_2O_{(l)} \rightleftharpoons HCO^-_{3\,(aq)} + H^+_{(aq)}$	Auto-dissociation
$HCO^-_{3\,(aq)} + OH^-_{(aq)} \rightleftharpoons CO^{2-}_{3\,(aq)} + H_2O_{(l)}$	

As the absorption process proceeds, bicarbonate ions may further react with hydroxide ions to produce carbonate ions (CO_3^{2-}). Nevertheless, the reaction network remains reversible and strongly depends on the local CO_2 concentration and solution alkalinity. Continuous injection of CO_2 shifts the reaction equilibrium toward bicarbonate formation, promoting the conversion of carbonate ions back to bicarbonate species. Consequently, bicarbonate becomes the dominant carbon-containing species as the absorption process approaches equilibrium. This behaviour is consistent with the

concentration distribution presented in Fig. 7 (b). the relatively uniform distribution of KHCO3 throughout both the axial and radial directions indicate that the reaction product is readily dissolved and transported within the liquid phase. Moreover, the widespread presence of bicarbonate species confirms that the absorbed CO_2 was not only physically dissolved but also chemically converted through reaction with hydroxide ions.

It is important to distinguish the aqueous-phase species predicted by the CFD model from the crystalline phases identified after product recovery. During reactive absorption, dissolved CO_2 reacts with OH− to form bicarbonate, while bicarbonate may further react with OH− to form carbonate under sufficiently alkaline conditions. Conversely, continued CO_2 absorption and decreasing alkalinity can shift carbonate-containing species toward bicarbonate. Thus, the carbonate–bicarbonate distribution evolves with local CO_2 loading and solution alkalinity. The $KHCO_3$ concentration shown in Fig. 7(b) therefore represents the aqueous-phase condition during absorption rather than the expected composition of the recovered crystalline solid.

The spatial distributions discussed above should be interpreted within the assumptions of the present Eulerian framework. In particular, the fixed 2.9 mm bubble diameter eliminates explicit coalescence and breakup effects, while the Higbie-based mass-transfer coefficient and enhancement-factor formulation represent closure-model predictions. Consequently, although the framework reproduces the measured transient CO_2 breakthrough response, the detailed hydrodynamic and mass-transfer fields remain dependent on the selected constitutive correlations and operating regime.

4.6 Product Characterization

Following reactive absorption, the liquid product was concentrated by evaporation at 110 °C prior to solid characterization. This recovery step represents a different chemical state from that described by the CFD simulation, which predicts aqueous-phase species during absorption. During evaporation, progressive water removal increases the concentration of dissolved carbonate species and promotes crystallization. In addition, bicarbonate may undergo partial thermal conversion according to

$$2KHCO3 \rightarrow K_2CO_3 + CO_2 + H_2O.$$

Previous thermal studies have established this decomposition pathway, while temperature-resolved XRD measurements indicate that transformation from KHCO3 toward K_2CO_3 can begin at approximately 110–120 °C under stepwise heating conditions [36], [37]. Because the present product-recovery step was conducted at 110 °C, partial conversion of bicarbonate during evaporation is therefore plausible. This provides a mechanistic explanation for the dominant K_2CO_3 phase together with residual KHCO3 detected in the recovered solid, without implying complete conversion of bicarbonate.

The recovered solid was subsequently characterized using X-ray diffraction (XRD) and scanning electron microscopy (SEM) to determine its crystalline-phase composition and morphology. These analyses provide complementary experimental evidence of carbonate/bicarbonate product formation after recovery but are not treated as direct quantitative validation of the CFD-predicted aqueous $KHCO_3$ concentration or hydrodynamic fields. Accordingly, the CFD and solid-characterization results should be interpreted as representing sequential stages of the overall absorption–recovery process rather than directly comparable chemical states.

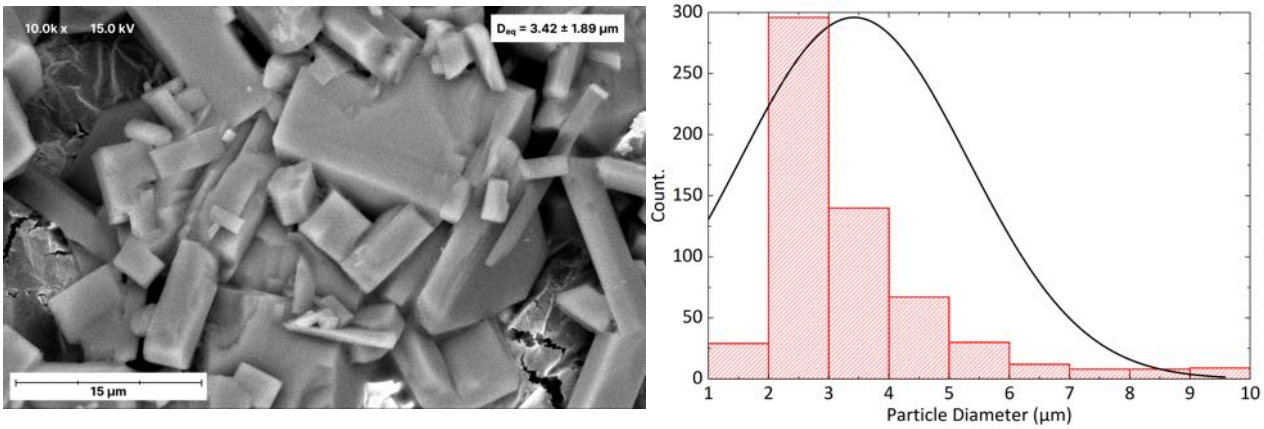

Fig. 8. Recovered solid-particle analysis: (a) SEM micrograph and (b) particle-size distribution

The observed morphology of the solid product recovered following reactive absorption and evaporation is illustrated in Fig. 8(a). SEM was employed to investigate the surface morphology and particle characteristics of the obtained solid phase. The micrograph was acquired at an accelerating voltage of 15 kV with a working distance of 6.87 mm. The SEM image revealed well-faceted particles exhibiting both plate-like and prismatic morphologies, with relatively smooth surfaces and clearly defined edges. The term "highly crystalline" is not inferred from SEM morphology alone; crystallinity is evaluated independently from the XRD pattern discussed below. The formation of well-defined crystal facets is consistent with anisotropic crystal growth, in which different crystallographic planes grow at different rates under supersaturated conditions [38]. In addition, significant agglomeration and crystal intergrowth were observed, which are consistent with particle attachment and secondary growth occurring during the concentration and crystallization stages of product recovery. The original SEM analysis and morphological observations are reported in the manuscript at the product-characterization stage.

Particle size analysis was performed using ImageJ software. The SEM image was first converted to Particle size analysis was performed using ImageJ software. The SEM image was first converted into a binary image using a threshold range of 75–165 based on pixel brightness. Particle dimensions were subsequently determined using the Feret diameter and bounding-rectangle functions, which were selected to represent the predominantly prismatic particle morphology. A total of 600 particles were analysed to obtain statistically representative results. The resulting particle-size distribution is shown in Fig. 8(b). The particle-size distribution exhibits a positively skewed profile, with most particles concentrated between 2 and 4 µm and a modal diameter of approximately 3 µm. The average particle size was 3.42 ± 1.89 µm, indicating a relatively broad size distribution with a coefficient of variation of 55.3%. The presence of a long tail extending toward larger particle sizes suggests that a limited fraction of particles experienced preferential growth, whereas most particles remained within the intermediate size range. This behaviour is consistent with the SEM observations, which revealed the coexistence of larger plate-like particles and smaller prismatic crystallites. Overall, the morphology and size distribution indicate heterogeneous crystal growth and agglomeration during solid recovery rather than providing a direct measure of the hydrodynamic or mass-transfer fields calculated by CFD.

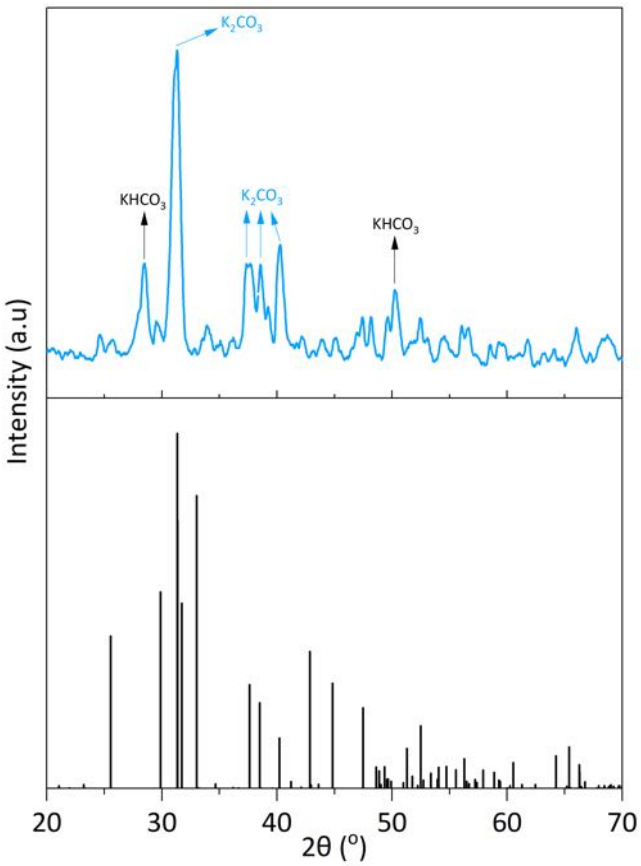

Fig. 9 X-Ray Diffraction Analysis

The X-Ray Diffraction pattern of the solid product obtained after reactive absorption and subsequent evaporation is presented in Fig. 9. Phase identification was performed using Match! software, and the diffraction peaks were matched with reference entry #96-210-7220 corresponding to crystalline K_2CO_3 [39 – 42]. The characteristic reflections are summarized in Table 5. The reference pattern corresponded closely with the experimental peaks, confirming the formation of crystalline potassium carbonate. The slight shifts in peak position (<0.2°) may be attributed to instrumental uncertainty and lattice imperfections within the recovered crystals. In addition to the dominant K_2CO_3 phase, diffraction peaks at approximately 28.52° and 50.28° were assigned to $KHCO_3$, indicating the coexistence of potassium bicarbonate within the recovered solid [43]. The experimental phase assignments and corresponding peak positions are reported in the original manuscript.

The predominance of K_2CO_3 in the XRD pattern is not inconsistent with the CFD prediction of KHCO3 formation. Rather, the two results describe different stages of the process. The CFD-predicted KHCO3 concentration represents aqueous-phase reaction products under bubble-column absorption conditions, before product recovery, whereas XRD characterizes the crystalline material remaining after evaporation at 110 °C. Because bicarbonate can partially transform to potassium carbonate during heating, part of the $KHCO_3$ present in the absorption solution may have been converted to K_2CO_3 during the recovery step. The residual KHCO3 reflections at approximately 28.52° and 50.28° are consistent with incomplete conversion at the applied recovery temperature, whereas the stronger K_2CO_3 reflections indicate that potassium carbonate became the dominant crystalline phase after evaporation. Temperature-resolved XRD evidence from the literature supports the onset of the KHCO3-to- K_2CO_3 crystalline transition in the vicinity of 110–120 °C.

Accordingly, the CFD and XRD results should be interpreted as complementary rather than directly equivalent measurements. The CFD simulation provides information on aqueous species formation and spatial distribution during reactive absorption, whereas XRD identifies the final crystalline phases after post-absorption thermal recovery. The observed K_2CO_3-rich solid containing residual $KHCO_3$ therefore supports the occurrence of carbonate–bicarbonate chemistry during the overall process, but it does not constitute a direct quantitative validation of the predicted aqueous $KHCO_3$ concentration.

Table 5
Peaks Comparison between Experiment and Reference

2θ Ref.	2θ Exp.	Species	Assignment
28.52°	28.52°	$KHCO_3$	Matched
31.34°	31.32°	K_2CO_3	Matched
37.64°	37.74°	K_2CO_3	Matched
38.49°	38.62°	K_2CO_3	Matched
40.22°	40.26°	K_2CO_3	Matched
50.28°	50.28°	$KHCO_3$	Matched

Furthermore, the diffraction pattern exhibited numerous sharp and intense reflections, indicating a high degree of crystallinity and long-range structural ordering in the recovered solid. The corresponding SEM observations revealed well-faceted prismatic particles with relatively smooth surfaces and distinct crystal edges, providing complementary morphological information on the solid formed during product recovery. Minor differences in relative XRD peak intensities compared with the reference pattern may be associated with preferred orientation arising from the anisotropic morphology of the crystalline particles. Taken together, SEM and XRD provide complementary post-recovery evidence of the morphology and crystalline-phase composition of the recovered product. XRD establishes the presence of carbonate/bicarbonate-containing crystalline phases, whereas SEM characterizes the particle morphology and size distribution developed during solid recovery. These analyses therefore support interpretation of product evolution across the absorption–recovery process but do not constitute direct validation of the CFD-predicted hydrodynamic fields or aqueous species concentrations.

5. Conclusion

This study establishes an integrated transient CFD framework for semi-batch CO_2–KOH reactive absorption by coupling Eulerian multiphase hydrodynamics, interfacial-force closures, Higbie penetration-based mass transfer, and reaction enhancement. The framework reproduced the experimental CO_2 breakthrough response with an R^2 of 0.986 and an RMSE of 0.003, while providing spatially resolved predictions of gas holdup, interfacial area, mass-transfer coefficient, and reactive-species evolution. The scientific contribution in integrating established formulations to reveal the mechanistic coupling between local hydrodynamics, interfacial transport, and chemical reaction during transient CO_2 absorption. The predicted aqueous $KHCO_3$ formation and the K_2CO_3-dominant solid identified after evaporation represent different stages of the absorption–recovery process, with XRD providing complementary evidence of the recovered carbonate/bicarbonate phases and SEM

characterizing the solid morphology rather than directly validating the CFD-predicted internal fields. Overall, the framework provides a mechanistically interpretable basis for analysing reactive bubble-column performance within the investigated operating range, while further validation and extension are required for different reactor scales, operating conditions, and absorbent systems. Future work should extend the present framework by incorporating bubble-size evolution through coalescence and breakup, independently validating the predicted hydrodynamic and mass-transfer fields, and evaluating its applicability across wider operating conditions and larger-scale or continuous bubble-column configurations.

Acknowledgement
The authors would like to express hearty gratefulness to the Fluid Mechanic and Mixing Laboratory research teams, Chemical Engineering Department, Sepuluh Nopember Institute of Technology (ITS). Big appreciation also given to Basis Informasi Penelitian dan Pengabdian Masyarakat (BIMA) foundation provided by Ministry of Education, Culture, Research, and Technology of the Republic of Indonesia for the financial support with official grant number 017/C3/DT.05.00/PL/2025 and 1308/PKS/ITS/2025.

References
[1] P. H. M. Feron, *Absorption-Based Post-Combustion Capture of Carbon Dioxide*. Woodhead Publishing, 2016.
[2] W. Zhang, Y. Yang, Y. Li, F. Li, and M. Luo, "Recent Progress on Integrated CO2 Capture and Electrochemical Upgrading," Sep. 01, 2023, *Academic Press*. doi: 10.1016/j.mtcata.2023.100006.
[3] J. Elfving, J. Kauppinen, M. Jegoroff, V. Ruuskanen, L. Järvinen, and T. Sainio, "Experimental Comparison of Regeneration Methods for CO2 Concentration from Air using Amine-Based Adsorbent," *Chemical Engineering Journal*, vol. 404, Jan. 2021, doi: 10.1016/j.cej.2020.126337.
[4] S. Ghavamipour, L. Vafajoo, G. Pourhossein, P. Parthasarathy, and G. McKay, "Post-Combustion CO2 Capturing by KOH Solution: An Experimental and Statistical Optimization Modeling Study," *Energy and Environment*, 2024, doi: 10.1177/0958305X241230944.
[5] A. M. Hissanaga, N. Padoin, and E. E. Paladino, "Mass Transfer Modeling and Simulation of a Transient Homogeneous Bubbly Flow in a Bubble Column," *Chem. Eng. Sci.*, vol. 218, Jun. 2020, doi: 10.1016/j.ces.2020.115531.
[6] N. Kantarci, F. Borak, and K. O. Ulgen, "Bubble Column Reactors," Jun. 2005. doi: 10.1016/j.procbio.2004.10.004.
[7] G. Besagni, N. Varallo, and R. Mereu, "Computational Fluid Dynamics Modelling of Two-Phase Bubble Columns: A Comprehensive Review," *Fluids*, vol. 8, no. 3, p. 91, Mar. 2023, doi: 10.3390/fluids8030091.
[8] J. Liu, P. Zhou, L. Liu, S. Chen, Y. Song, and H. Yan, "CFD Modeling of Reactive Absorption of CO2 in Aqueous NaOH in a Rectangular Bubble Column: Comparison of mass Transfer and Enhancement Factor model," *Chem. Eng. Sci.*, vol. 230, Feb. 2021, doi: 10.1016/j.ces.2020.116218.
[9] C. Li, Y. Cui, X. Shi, J. Gao, and X. Lan, "CFD Simulation of Mass Transfer in Bubble Columns: Detailed Study of Mass Transfer Models," *Chem. Eng. Sci.*, vol. 264, Dec. 2022, doi: 10.1016/j.ces.2022.118173.
[10] J. Mach, J. Wiens, J. Adjaye, A. A. Donaldson, and A. Macchi, "Effect of Pressure on the Drag Coefficient of Individual Bubbles in a Contaminated Polydisperse Swarm," *Chem. Eng. Sci.*, vol. 223, Sep. 2020, doi: 10.1016/j.ces.2020.115728.
[11] L. Zhang, Z. Zhou, J. Deng, and X. Shao, "A Numerical Study on the Drag Law of a Gas Bubble using Dynamic Body Force Method," *Physics of Fluids*, vol. 33, no. 6, Jun. 2021, doi: 10.1063/5.0055646.
[12] M. Krauß and R. Rzehak, "Reactive absorption of CO2 in NaOH: An Euler-Euler simulation study," *Chem. Eng. Sci.*, vol. 181, pp. 199–214, May 2018, doi: 10.1016/j.ces.2018.01.009.
[13] M. A. Taborda, R. Kipping, U. Hampel, and M. Sommerfeld, "Advanced Analysis of Bubble Columns: Comparison of Euler/Lagrange Simulations and Experiments under CO2 Chemisorption Conditions," *Chemical Engineering Research and Design*, vol. 170, pp. 389–405, Jun. 2021, doi: 10.1016/j.cherd.2021.04.020.
[14] K. I. Kuznetsov, S. V. Skorodumov, and P. P. Granchenko, "Measurements of the Dynamic Viscosity and Density of KOH Solutions at Atmospheric Pressure," *High Temperature*, vol. 58, no. 6, pp. 806–811, Nov. 2020, doi: 10.1134/S0018151X20060127.

[15] D. Parkhurst and C. Appelo, "Description of Input and Examples for PHREEQC Version 3-A Computer Program for Speciation, Batch-Reaction, One-Dimensional Transport, and Inverse Geochemical Calculations," in *Modelling Techniques*, 6th ed., 2013, ch. 43. [Online]. Available: http://www.hydrochemistry.eu

[16] G. F. Versteeg and W. P. M. van Swaaij, "Solubility and Diffusivity of Acid Gas (CO2, N2O) in Alkalolamine Solutions," *American Chemical Society*, 1988.

[17] R. Sander, "Compilation of Henry's Law Constants (version 5.0.0) for Water as Solvent," Oct. 06, 2023, *Copernicus Publications*. doi: 10.5194/acp-23-10901-2023.

[18] I. Khan, M. Wang, Y. Zhang, W. Tian, G. Su, and S. Qiu, "Two-Phase Bubbly Flow Simulation using CFD Method: A Review of Models for Interfacial Forces," *Progress in Nuclear Energy*, vol. 125, Jul. 2020, doi: 10.1016/j.pnucene.2020.103360.

[19] A. Tomiyama, "Struggle with Computational Bubble Dynamics," *Multiphase Science and Technology*, vol. Volume 10, 1998, doi: 10.1615/MultScienTechn.v10.i4.40.

[20] A. Tomiyama, H. Tamai, I. Zun, and S. Hosokawa, "Transverse Migration of Single Bubbles in Simple Shear Flow," *Chem. Eng. Sci.*, vol. 57, pp. 1849–1858, Sep. 2002, doi: 10.1016/S0009-2509(02)00085-4.

[21] A. Burns, T. Frank, I. Hamill, and J.-M. Shi, "The Favre Averaged Drag Model for Turbulent Dispersion in Eulerian Multi-Phase Flows," in *Conf. on Multiphase Flow, ICMF2004*, Sep. 2004.

[22] T. Frank, "Advances in Computational Fluid Dynamics (CFD) of 3-Dimensional Gas-Liquid Multiphase Flows," Wiesbaden,Germany: In Proceedings of the NAFEMS Seminar: Simulation of Complex Flows (CFD)–Applications and Trends, Apr. 2005.

[23] T. Ziegenhein, R. Rzehak, E. Krepper, and D. Lucas, "Numerical Simulation of Polydispersed Flow in Bubble Columns with the Inhomogeneous Multi-Size-Group Model," *Chem. Ing. Tech.*, vol. 85, no. 7, pp. 1080–1091, Jul. 2013, doi: 10.1002/cite.201200223.

[24] J. Michelson *et al.*, "Modeling of a Bubble Column for CO2 Removal by Absorption with NaOH," *Chem. Eng. Commun.*, vol. 211, no. 4, pp. 571–581, 2024, doi: 10.1080/00986445.2023.2261105.

[25] R. Higbie, "The Rate of Absorption of Pure Gas into a Still Liquid during Short Periode of Exposure," 1935.

[26] A. C. Lochiel and P. H. Calderbank, "Mass Transfer in the Continuous Phase Around Axisymmetric Bodies of Revolution," *Chem. Eng. Sci.*, vol. 19, no. 7, pp. 471–484, 1964, doi: https://doi.org/10.1016/0009-2509(64)85074-0.

[27] M. Krauβ and R. Rzehak, "Reactive absorption of CO2 in NaOH: Detailed study of enhancement factor models," *Chem. Eng. Sci.*, vol. 166, pp. 193–209, 2017, doi: 10.1016/j.ces.2017.03.029.

[28] W. J. DeCoursey, "Absorption with Chemical Reaction: Development of a New Relation for the Danckwerts Model," *Chem. Eng. Sci.*, vol. 29, no. 9, pp. 1867–1872, 1974, doi: https://doi.org/10.1016/0009-2509(74)85003-7.

[29] Q. Hu *et al.*, "A Critical Review of Breakthrough Models with Analytical Solutions in a Fixed-Bed Column," Mar. 01, 2024, *Elsevier Ltd*. doi: 10.1016/j.jwpe.2024.105065.

[30] G. P. Gakis, D. Marinos, I. G. Aviziotis, E. Balomenos, A. G. Boudouvis, and D. Panias, "An Integrated, CFD-Based, Analysis of Carbonation in a Stirred Tank Reactor," *Materials*, vol. 18, no. 7, Apr. 2025, doi: 10.3390/ma18071535.

[31] A. N. Mahmood, A. A. Abdulrahman, L. S. Sabri, A. J. Sultan, H. S. Majdi, and M. H. Al-Dahhan, "Flow Regimes in Bubble Columns with and without Internals: A Review," *Fluid Dynamics and Materials Processing*, vol. 20, no. 2, pp. 239–256, 2023, doi: https://doi.org/10.32604/fdmp.2023.028015.

[32] W.-D. Deckwer, Y. Loulsl, A. Zaldl, and M. Ralek, "Hydrodynamic Properties of the Fischer-Tropsch Slurry Process," Press, 1980.

[33] J. Chen and C. S. Brooks, "Experiments and CFD Simulation of Mass Transfer and Hydrodynamics in a Cylindrical Bubble Column," *Chem. Eng. Sci.*, vol. 234, Apr. 2021, doi: 10.1016/j.ces.2020.116435.

[34] X. Shen, Z. Jia, H. Zhang, and T. Wang, "Numerical Simulation of Volumetric Mass Transfer Coefficients in Slurry Bubble Columns with a CFD-PBM Coupled Model," *Chem. Eng. Sci.*, vol. 318, Dec. 2025, doi: 10.1016/j.ces.2025.122153.

[35] A. Lazou *et al.*, "CO2 Absorption in NaOH-Na2CO3 Solutions: Combined CFD and Thermodynamics-Based, Experimentally Validated Analysis," *Chem. Eng. Sci.*, vol. 327, Jun. 2026, doi: 10.1016/j.ces.2026.123613.

[36] I. C. Hisatsune and T. Adl, "Thermal decomposition of potassium bicarbonate," *J. Phys. Chem.*, vol. 74, no. 15, pp. 2875–2877, Jul. 1970, doi: 10.1021/j100709a004.

[37] D. Salehzadeh, B. Elahi, J. E. ten Elshof, G. Brem, and M. Mehrali, "Porous potassium carbonate granules with enhanced diffusion kinetics for thermochemical heat storage," *Chemical Engineering Journal*, vol. 497, p. 154560, Oct. 2024, doi: 10.1016/j.cej.2024.154560.

[38] B. Elahi, D. Salehzadeh, W. M. de Vos, N. Shahidzadeh, G. Brem, and M. Mehrali, "Boosting Stability of K2CO3 Granules for Thermochemical Heat Storage Applications through Innovative Membrane Encapsulation," *Chemical Engineering Journal*, vol. 500, Nov. 2024, doi: 10.1016/j.cej.2024.157042.

[39] H. Y. Becht and S. R., "A Monoclinic High-Temperature Modification of Potassium Carbonate," *Acta Crystallogr. B*, vol. 32, no. 12, pp. 3344–3346, 1976, doi: 10.1107/s0567740876010303.

[40] Q. Ye, X. Wang, and Y. Lu, "Kinetic Behavior of Potassium Bicarbonate Crystallization in a Carbonate-Based CO2 Absorption Process," *Chemical Engineering Research and Design*, vol. 93, pp. 136–147, Jan. 2015, doi: 10.1016/j.cherd.2014.06.012.

[41] N. Mazur, H. Huinink, H. Fischer, P. Donkers, and O. Adan, "Accelerating the Reaction Kinetics of K2CO3 through the Addition of CsF in the View of Thermochemical Heat Storage," *Solar Energy*, vol. 242, pp. 256–266, Aug. 2022, doi: 10.1016/j.solener.2022.07.023.

[42] A. I. Shkatulov, J. Houben, H. Fischer, and H. P. Huinink, "Stabilization of K2CO3 in Vermiculite for Thermochemical Energy Storage," *Renew. Energy*, vol. 150, pp. 990–1000, May 2020, doi: 10.1016/j.renene.2019.11.119.

[43] Y. Wu, M. S. Alivand, G. Hu, G. W. Stevens, and K. A. Mumford, "Nucleation Kinetics of Glycine Promoted Concentrated Potassium Carbonate Solvents for Carbon Dioxide Absorption," *Chemical Engineering Journal*, vol. 381, Feb. 2020, doi: 10.1016/j.cej.2019.122712.